Science Advances

$\blacktriangleright$AAAS

Supplementary Materials for

An ion redistributor for dendrite-free lithium metal anodes

Chen-Zi Zhao, Peng-Yu Chen, Rui Zhang, Xiang Chen, Bo-Quan Li, Xue-Qiang Zhang, Xin-Bing Cheng*, Qiang Zhang*

*Corresponding author. Email: cxb12@mails.tsinghua.edu.cn (X.-B.C.); zhang-qiang@mails.tsinghua.edu.cn (Q.Z.)

This PDF file includes:

Fig. S19. XPS spectra of the deposited Li metal anode surface with the routine PP separator in DOL/DME electrolytes.

Fig. S20. Voltage hysteresis of Li│Li pouch cells with EC/DEC electrolytes at a current density of 0.25 mA cm^{-2}.

Fig. S21. Morphology and cycling performances of the separator with PAN layer of lower ionic conductivity compared with the LLZTO composite separator of the LLZTO film.

Fig. S22. Morphology of the composite separator with Al_2O_3 layer.

Fig. S23. Cycling performances of the composite separator with Al_2O_3 and LLZTO coating layer.

Fig. S24. Cycling performances of the composite separator with Al_2O_3 layer and LLZTO coating layers.

Fig. S25. Electrochemical impedances of Li│Li symmetrical cells in EC/DEC electrolytes at 1.0 mA cm^{-2}.

Fig. S26. Ion transportation behaviors in the composite separator with a LLZTO ion conductive layer and a Li-ion insulator layer when limited liquid electrolytes are adopted.

Fig. S27. Atomic force microscopy analysis of the LLZTO composite separator and the Al_2O_3 composite separator.

Fig. S28. Morphology and cycling performances of the separator with a thicker LLZTO film (30 μm) to redistribute Li ions compared with the LLZTO composite separator of the 5-μm LLZTO film.

Fig. S29. Morphology and cycling performances of the separator with isolated LLZTO particles compared with the LLZTO composite separator of the 5-μm LLZTO film.

Table S1. Statistics of the concentration of Li ions beneath the routine PP separator and the composite separator at $y = 9.0$ μm.

Table S2. Element atomic percentage of Li metal anode surface with the LLZTO composite separator and the routine PP separator obtained from XPS spectra.

Supplementary Materials

1. Supplementary Figures

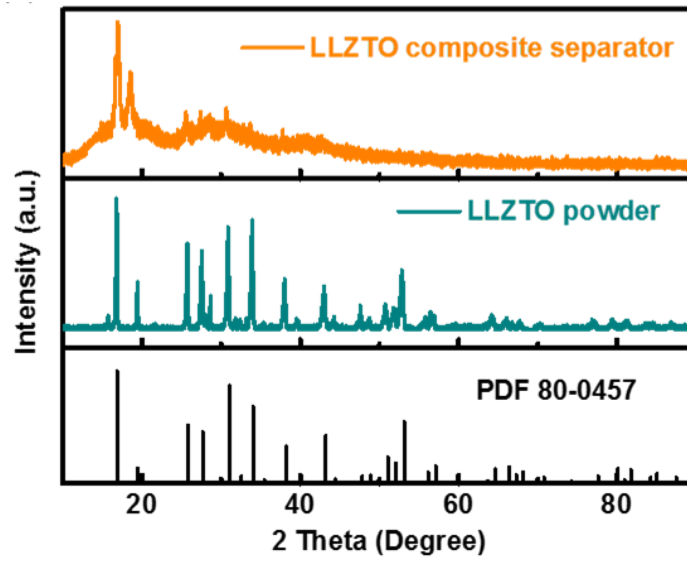**Fig. S1. XRD patterns of the LLZTO composite separator (orange), LLZTO powder (cyan), and the powder diffraction file (PDF) of $Li_5La_2Nb_2O_{12}$.**
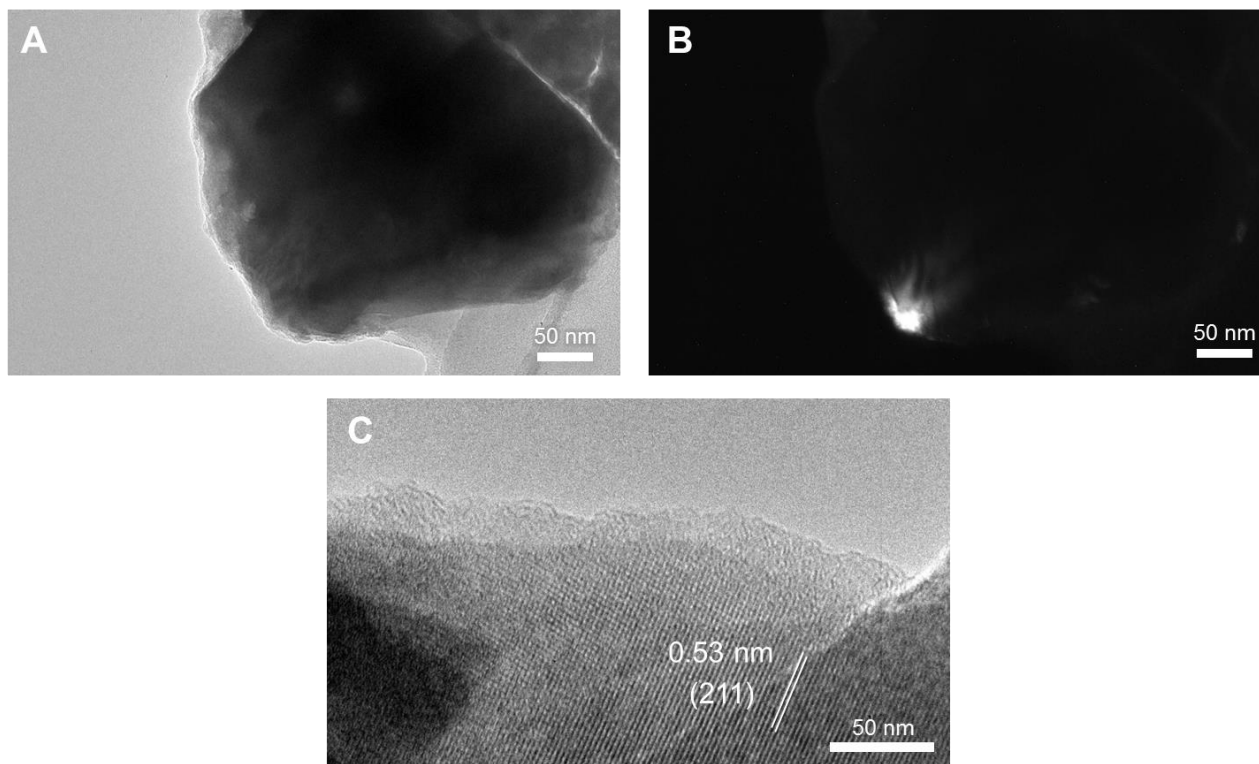
Fig. S2. TEM images of the LLZTO ceramic powders. (**A**) bright field, (**B**) dark field, and (**C**) high resolution TEM images of the LLZTO ceramic powders.
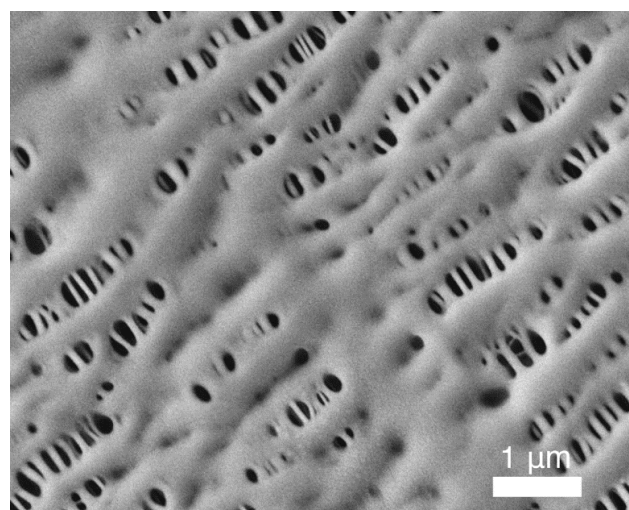

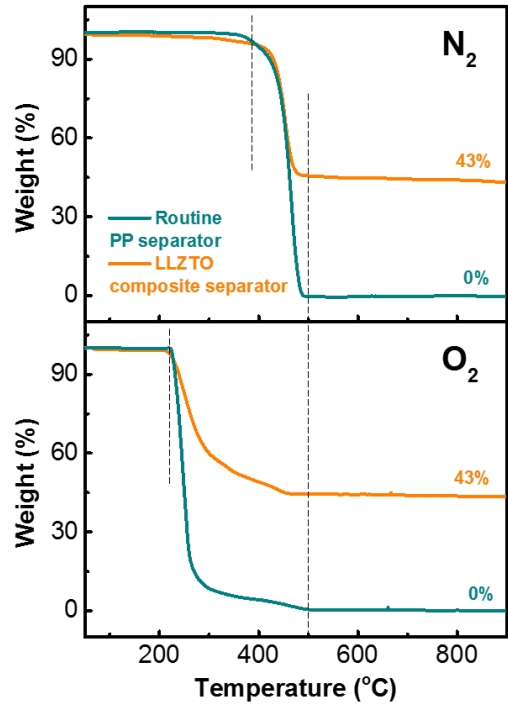**Fig. S3. SEM image for the surface of commercial PP separator (Celgard 2400).**

Fig. S4. TGA curves of routine PP separator (cyan) and LLZTO composite separator (orange) in nitrogen or oxygen atmosphere.
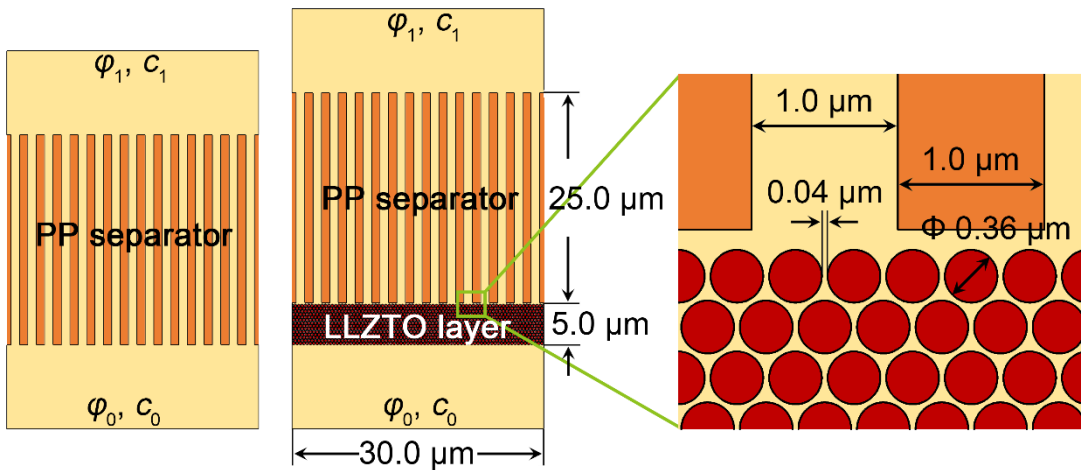
Fig. S5. FEM models for the routine PP separator (without LLZTO layer) and the composite separator (with LLZTO layer).
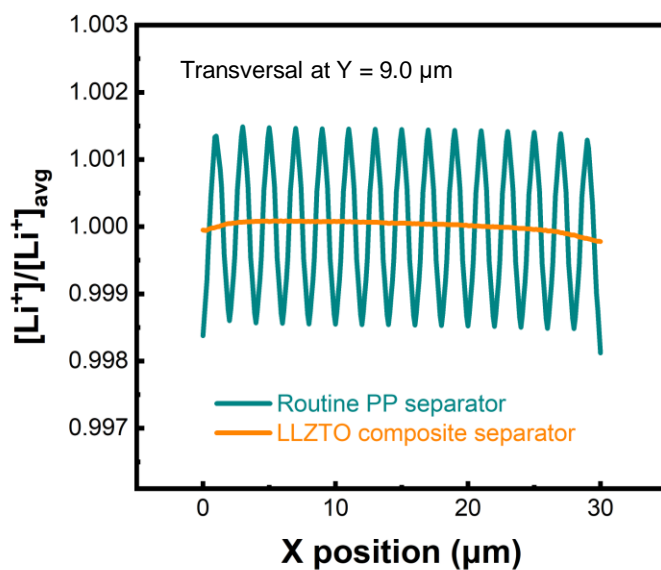
Fig. S6. The relative concentration of Li ions beneath the routine PP separator (cyan line) and the composite separator (orange line) at *y* = 9.0 μm in the FEM simulation results (Fig. 3, A and B).

$[Li^+]_{avg}$ is the average concentration at Y = 9.0 μm for each separator.

Fig. S7. Schematic illustration of the electrolytic cells designed for electrochemical deposition to avoid the effect of stress.

Fig. S8. Schematic illustration of the coin cells designed for electrochemical deposition to avoid the effect of stress and maintain the close contact between LLZTO ion redistributors and electrodes.
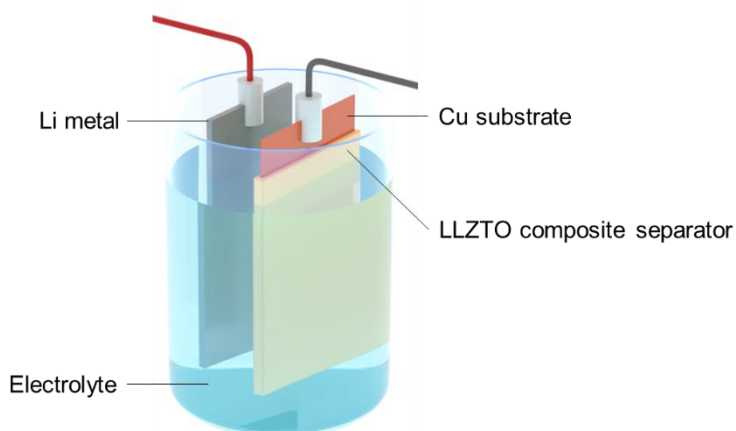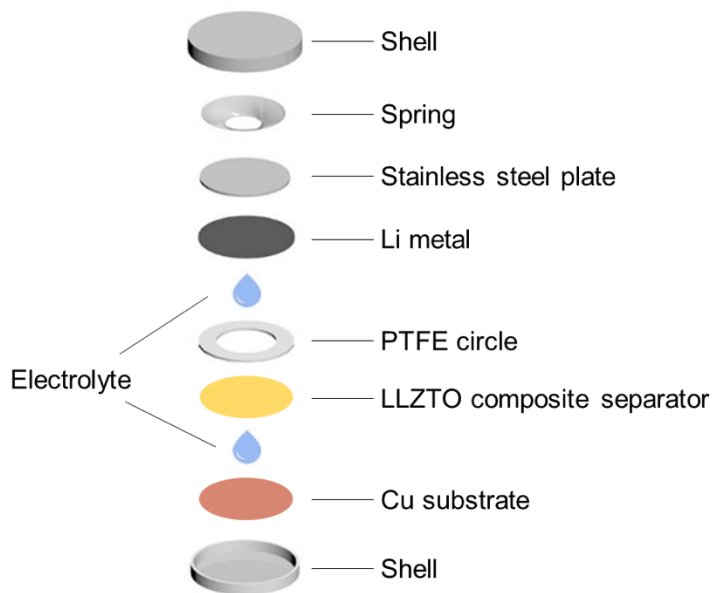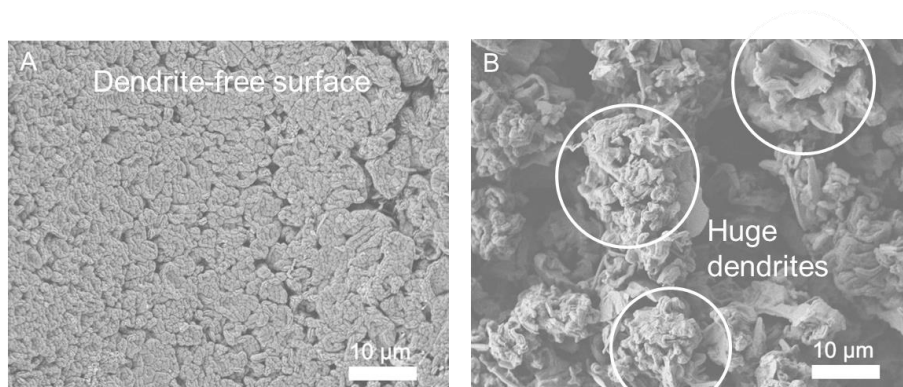

Fig. S9. SEM images of Li metal deposits in coin cells with PTFE circle through (**A**) LLZTO composite separator and (**B**) routine PP separator.
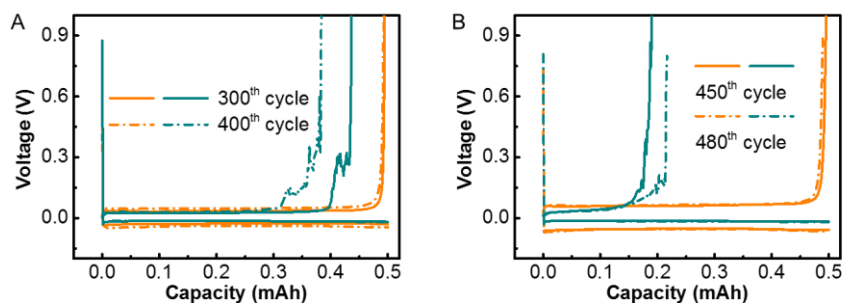
Fig. S10. Charge and discharge voltage profiles of Li|Cu cells at (**A**) 300th cycle (solid line) / 400th cycle (dashed line) and (**B**) 450th cycle (solid line) / 480th cycle (dashed line) with LLZTO composite separator (orange) and routine PP separator (cyan).
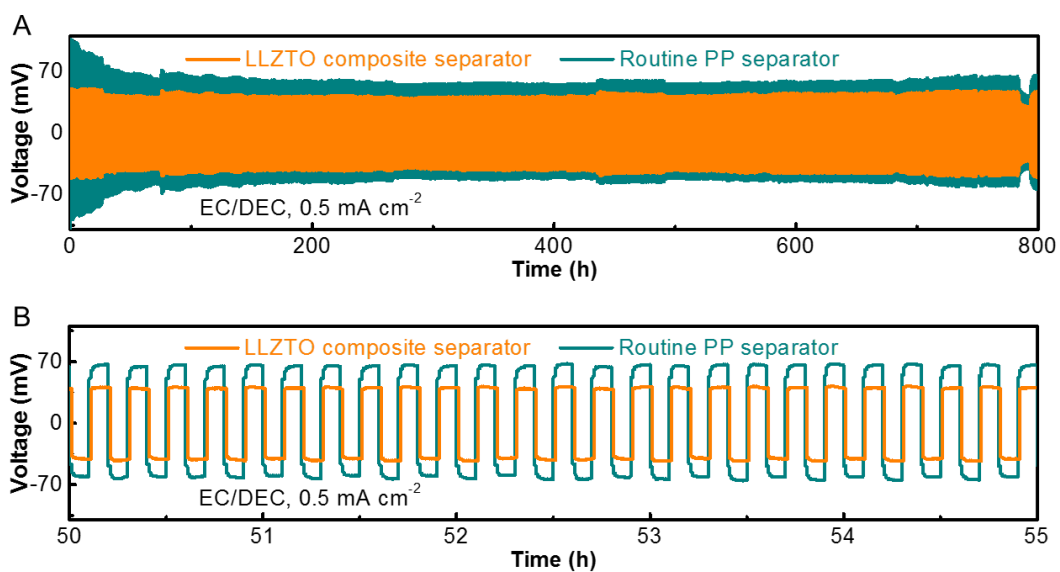
Fig. S11. **Voltage profiles for Li|Li symmetric cells using carbonate-based EC/DEC electrolytes at a current density of 0.5 mA cm^{-2}.** (**A**) Voltage profiles and (**B**) enlarged voltage profiles for Li–Li symmetric cells using carbonate-based EC/DEC electrolytes at a current density of 0.5 mA cm^{-2}.
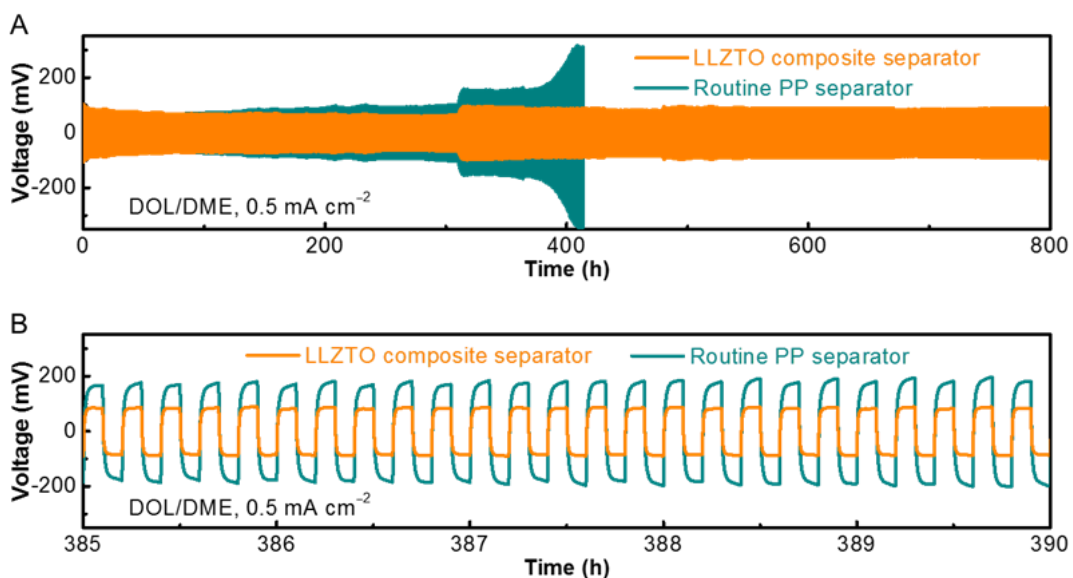
Fig. S12. Voltage profiles for Li|Li symmetric cells using ether-based DOL/DME electrolytes at a current density of 0.5 mA cm^{-2}. (**A**) Voltage profiles and (**B**) enlarged voltage profiles for Li–Li symmetric cells using ether-based DOL/DME electrolytes at a current density of 0.5 mA cm^{-2}.
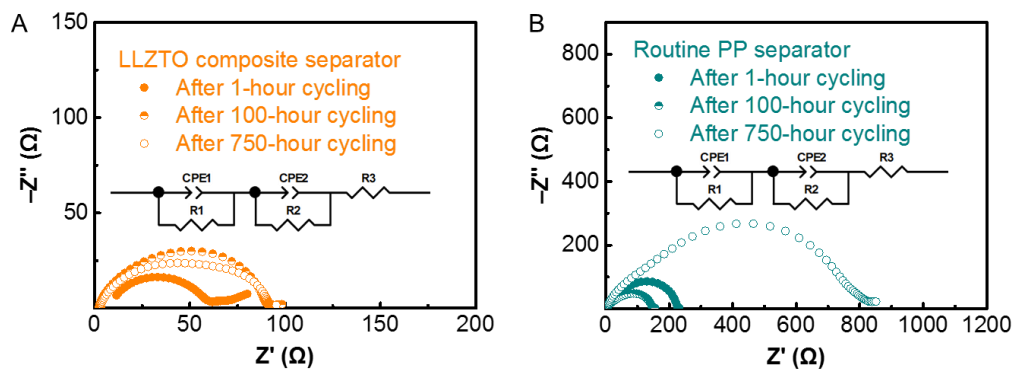

Fig. S13. Impedance spectra of Li|Li cells with (**A**) LLZTO composite separators (yellow) and (**B**) routine PP separators (cyan). Insert is the equivalent circuit for simulation. R1 and R2 stand for interfaces in Li–Li cells. R3 stands for bulk electrolyte resistance. CPE1 and CPE2 stand for the constant phase element.
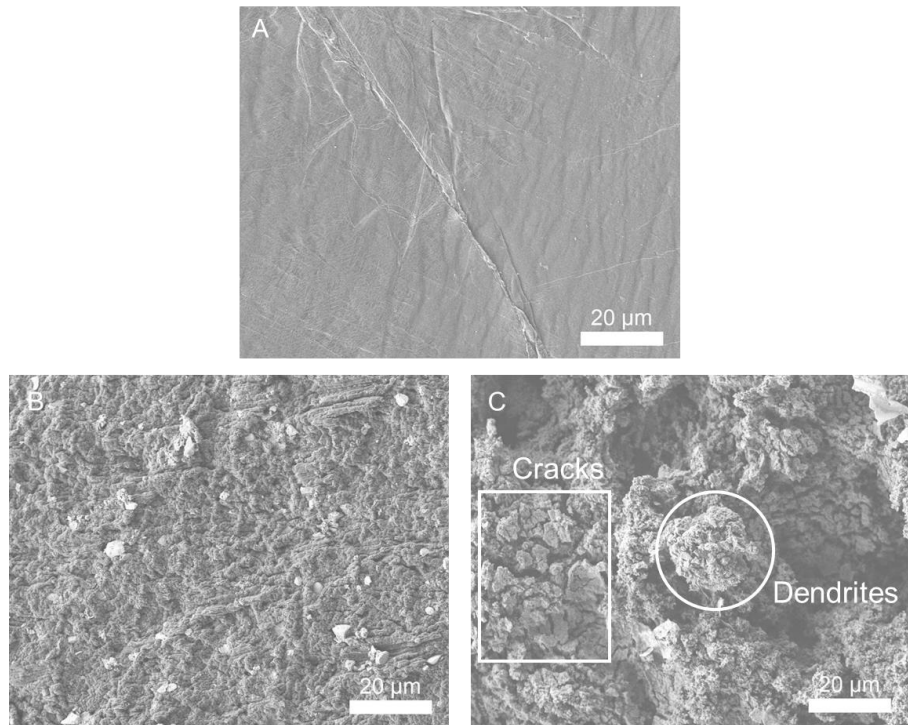
Fig. S14. SEM images of Li metal electrodes in Li|Li symmetric cells (**A**) before cycling and after cycling with (**B**) LLZTO composite separator and (**C**) routine PP separator.
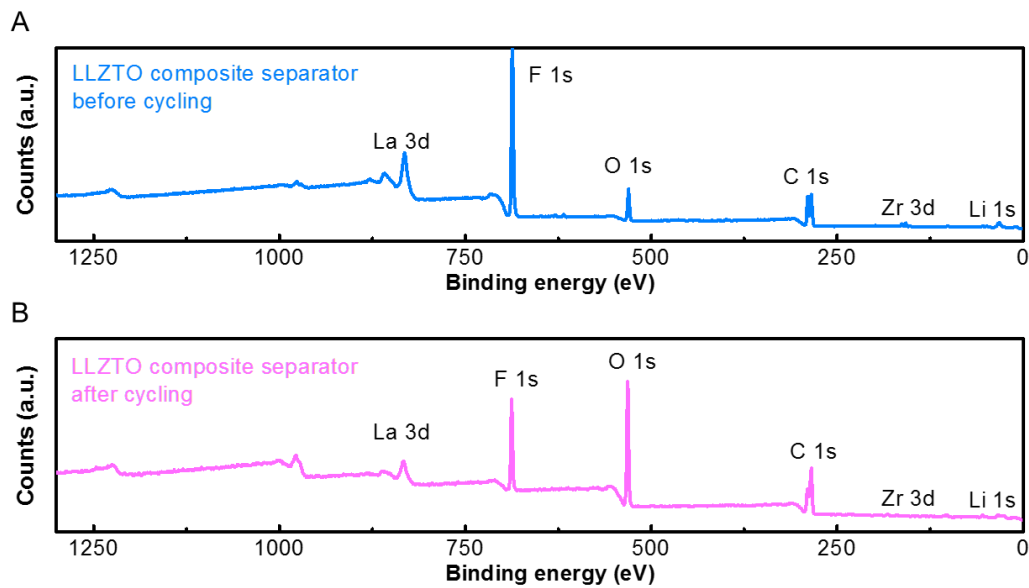
Fig. S15. XPS survey of LLZTO layer on composite separators (**A**) before and (**B**) after cycling.
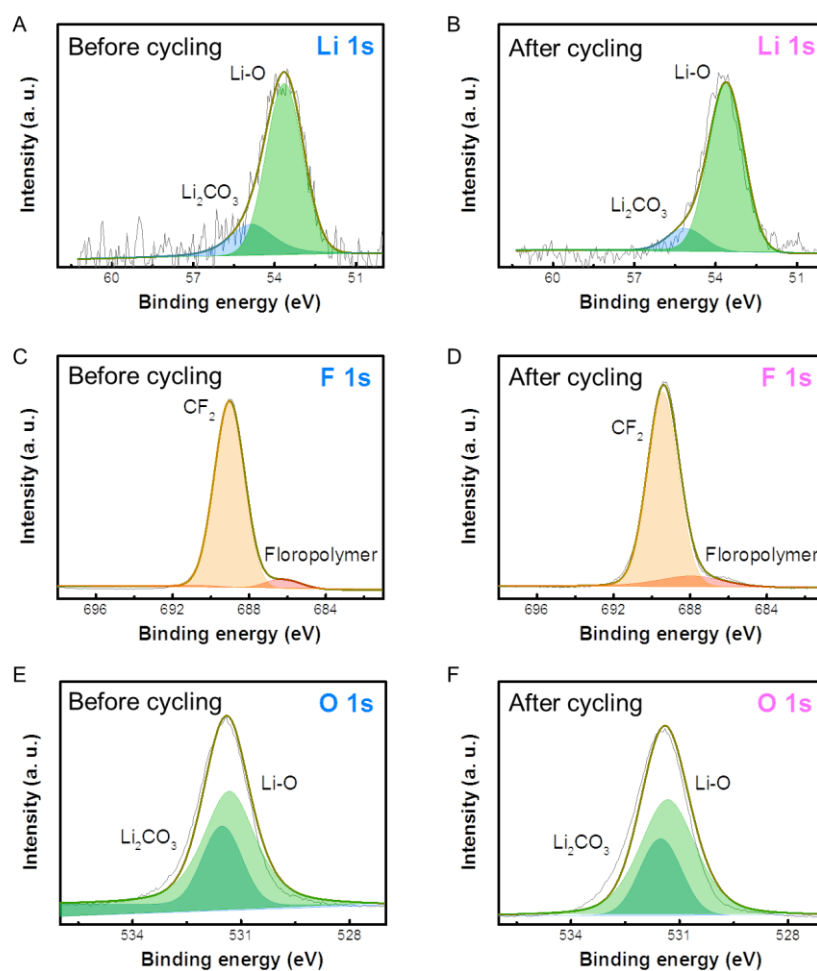
Fig. S16. XPS spectra of LLZTO layer on composite separators (**A**, **C**, **E**) before and (**B**, **D**, **F**) after cycling.
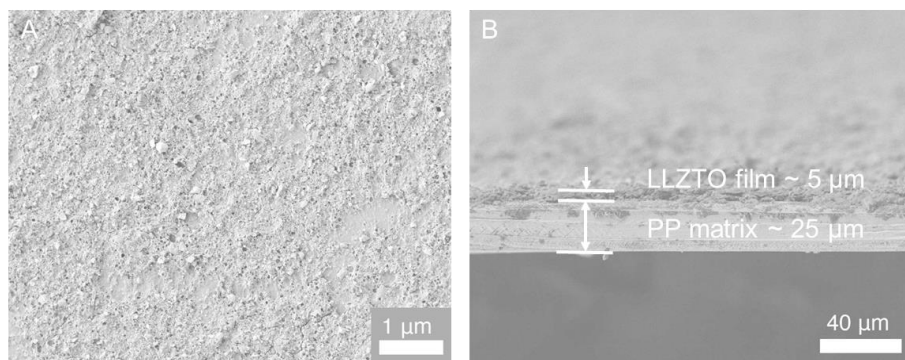
Fig. S17. Morphological characterizations of the LLZTO composite separator after cycling. (**A**) The surface image of composite separators after cycling. (**B**) A cross-section image of the composite separator showing an overall view consisting of LLZTO film and PP matrix.

Fig. S18. XPS spectra of the deposited Li metal anode surface with the LLZTO composite separator in DOL/DME electrolytes.
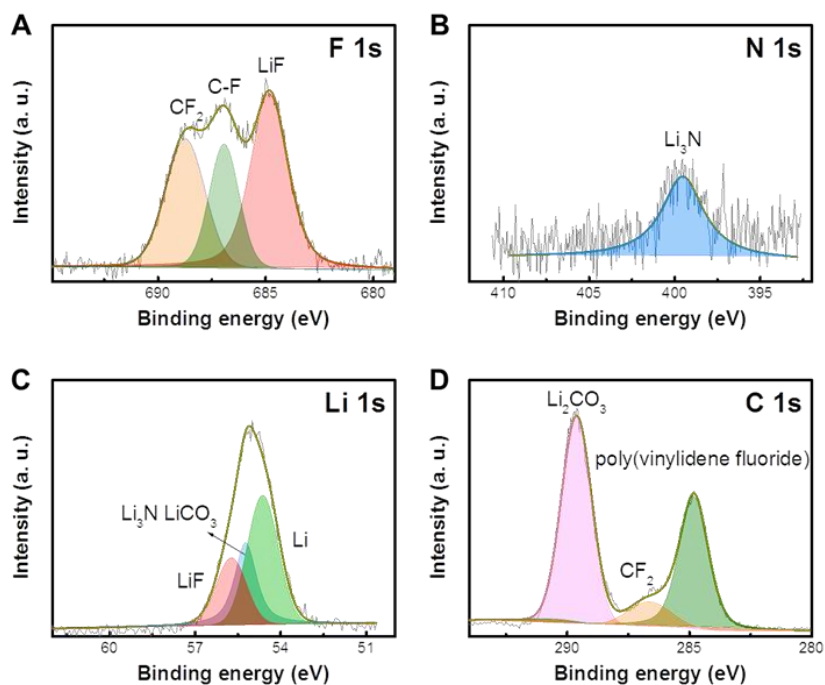
Fig. S19. XPS spectra of the deposited Li metal anode surface with the routine PP separator in DOL/DME electrolytes.
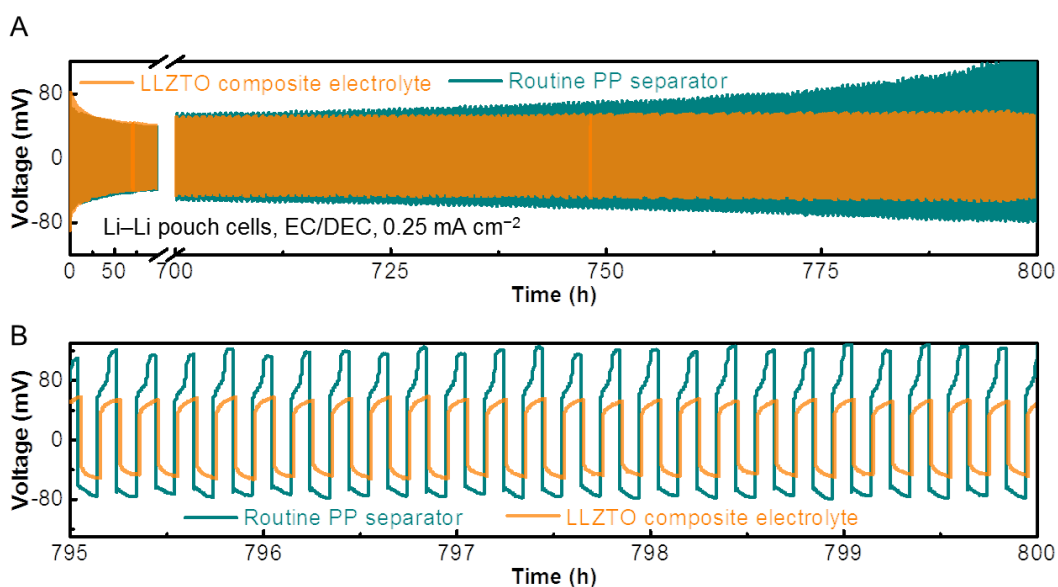
Fig. S20. Voltage hysteresis of Li│Li pouch cells with EC/DEC electrolytes at a current density of 0.25 mA cm⁻². (**A**) Voltage hysteresis and (**B**) enlarged voltage hysteresis of Li–Li pouch cells with EC/DEC electrolytes at a current density of 0.25 mA cm^{-2}.

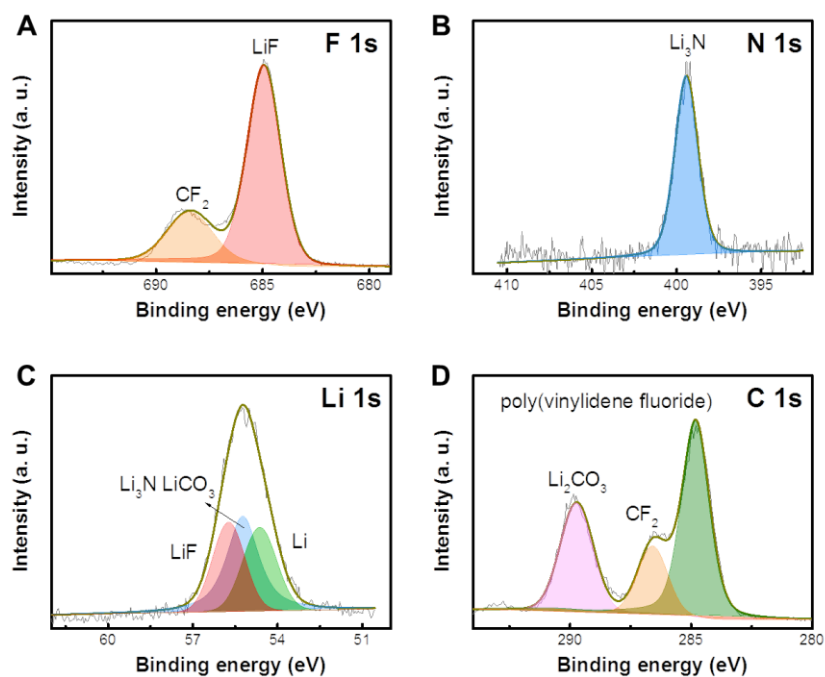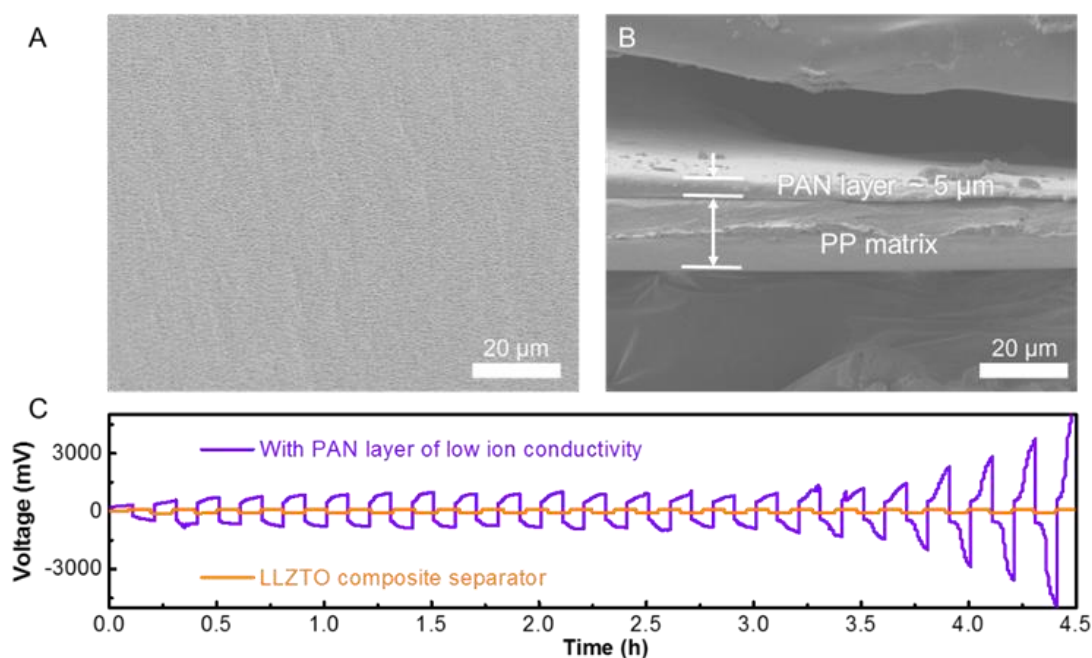**Fig. S21. Morphology and cycling performances of the separator with PAN layer of lower ionic conductivity compared with the LLZTO composite separator of the LLZTO film.** (**A**) The SEM images of the surface of the separator with transparent PAN layer, (**B**) A cross-section of the separator exhibiting an overall view consisting of PAN layer and PP matrix. (**C**) Voltage profiles for Li–Li symmetric cells using ether-based DOL/DME electrolytes at a current density of 1.0 mA cm^{-2}.
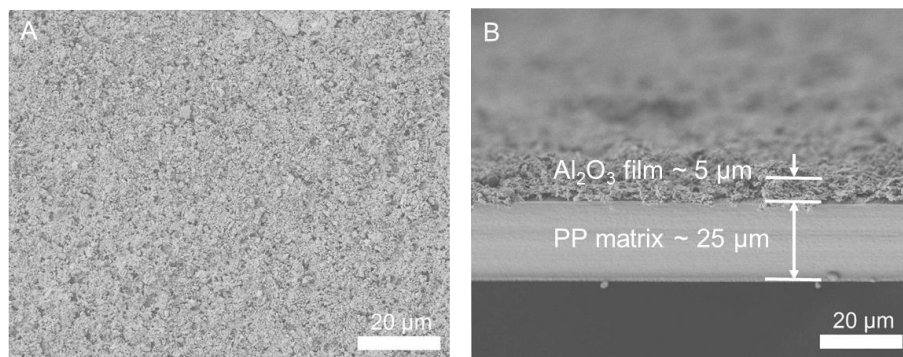
Fig. S22. Morphology of the composite separator with Al₂O₃ layer. (**A**) The SEM image of the surface of the separator with Al$_2$O$_3$ layer. (**B**) A cross-section image of the separator exhibiting an overall view consisting of Al$_2$O$_3$ layer and PP matrix.
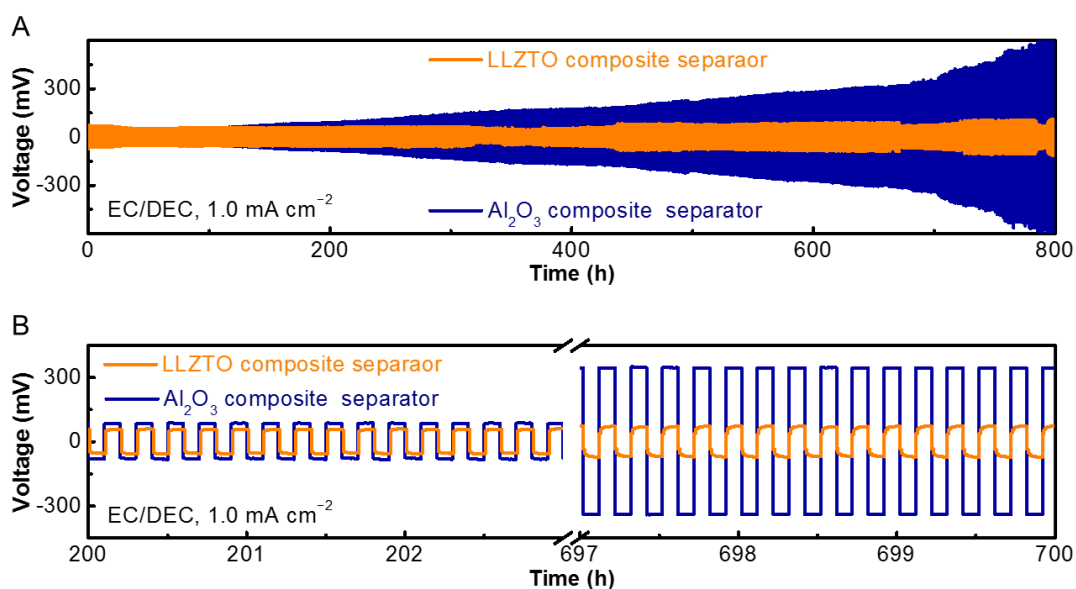
Fig. S23. Cycling performances of the composite separator with Al₂O₃ and LLZTO coating layer. (**A**) Voltage profiles and (**B**) enlarged voltage profiles for Li–Li symmetric cells using carbonate-based EC/DEC electrolytes at a current density of 1.0 mA cm^{-2}/0.1 mAh cm^{-2}.
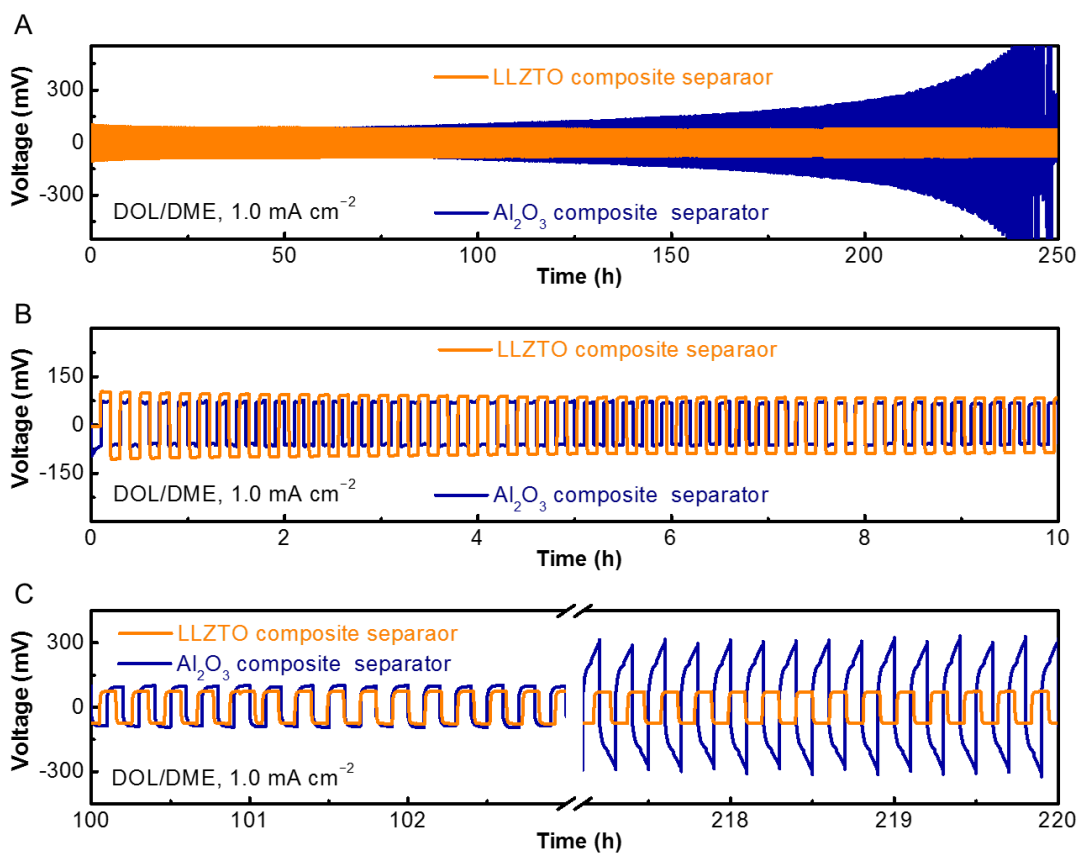
Fig. S24. Cycling performances of the composite separator with Al₂O₃ layer and LLZTO coating layers. (**A**) Voltage profiles and (**B**, **C**) enlarged voltage profiles for Li–Li symmetric cells using ether-based DOL/DME electrolytes at a current density of 1.0 mA cm^{-2}/0.1 mAh cm^{-2}.
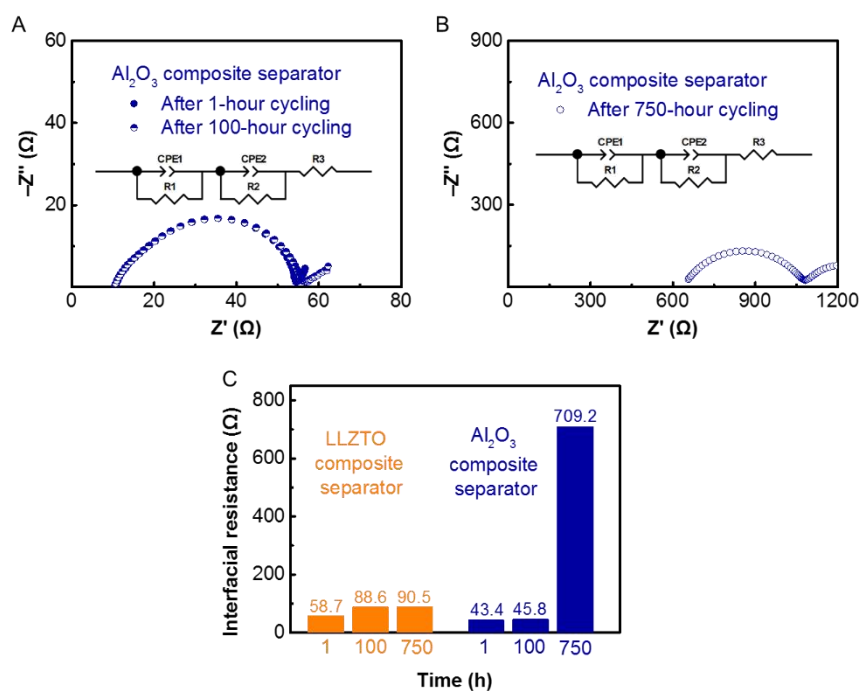
**Fig. S25. Electrochemical impedances of Li│Li symmetrical cells in EC/DEC electrolytes at 1.0 mA cm^{-2}.** Impedance spectra of Li–Li cells with Al_2O_3 composite separator after (**A**) 1-hour, 100-hour and (**B**) 750-hour cycling. Insert is the equivalent circuit for simulation. R1 and R2 stand for interfaces in Li–Li cells. R3 stands for bulk resistance. CPE1 and CPE2 stand for the constant phase elements. (**C**) Interfacial resistance in Li–Li cells calculated from impedance spectra after 1-, 100-, and 750-hour cycling.
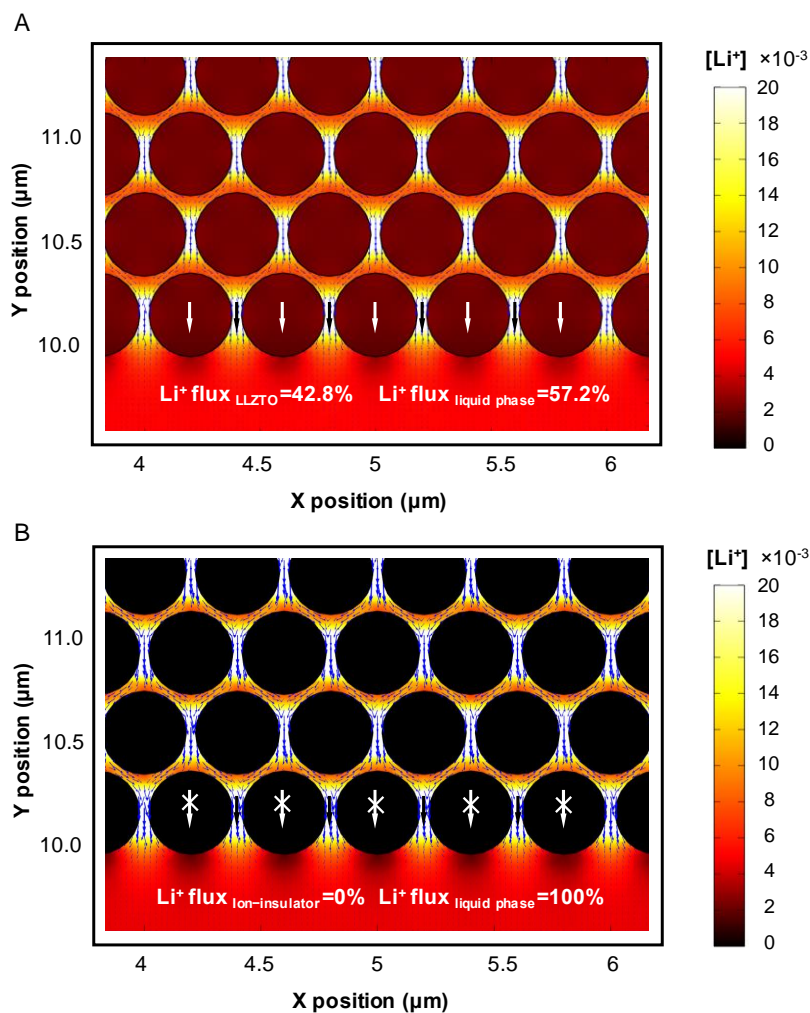
Fig. S26. Ion transportation behaviors in the composite separator with a LLZTO ion conductive layer and a Li-ion insulator layer when limited liquid electrolytes are adopted. The distribution of Li-ion flux beneath (A) the LLZTO layer and (B) a Li-ion-insulator layer such as Al_2O_3 ceramic layer. Colors in the graph represent the concentration of Li ions ($[Li^+]$).

Fig. S27. Atomic force microscopy analysis of the LLZTO composite separator and the Al₂O₃ composite separator. (**A**, **B**) AFM topological height images, (**C**, **D**) modulus map and (**E**, **F**) force curves of (A, C, E) LLZTO composite separator and (B, D, F) Al₂O₃ composite separator.
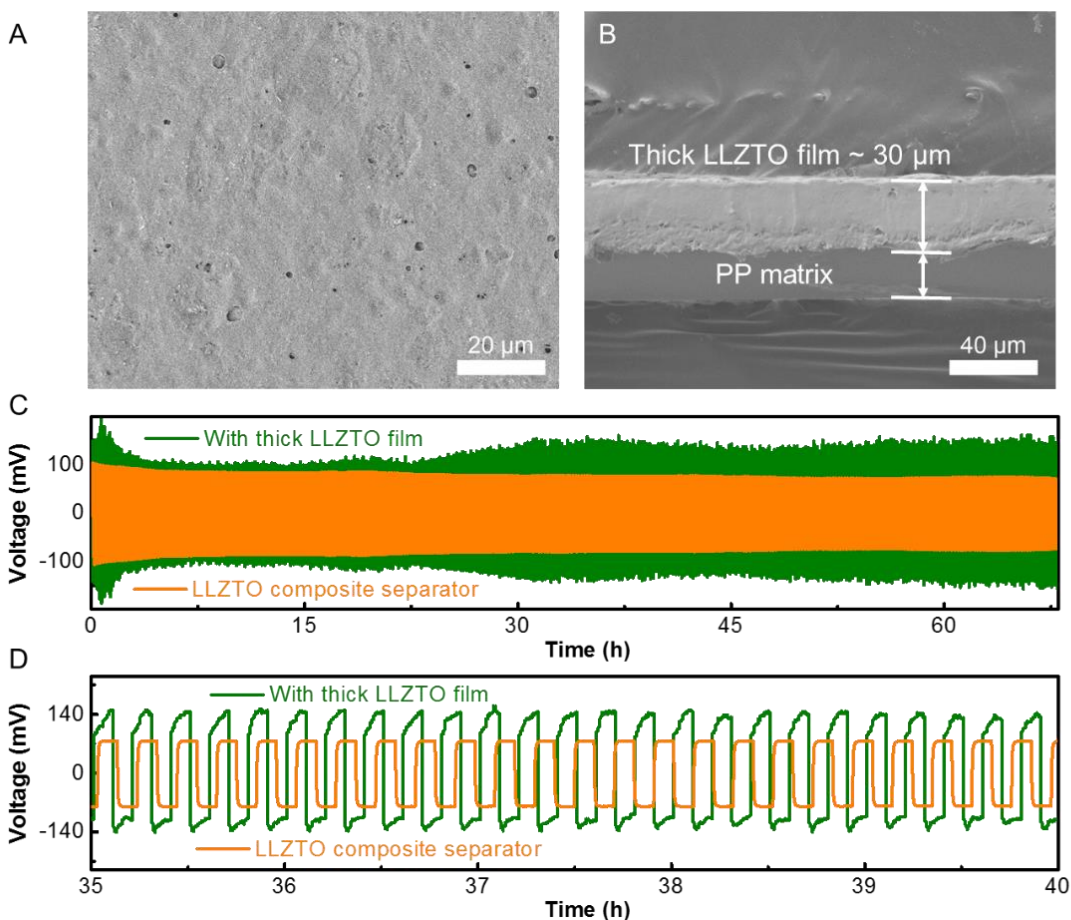
Fig. S28. Morphology and cycling performances of the separator with a thicker LLZTO film (30 μm) to redistribute Li ions compa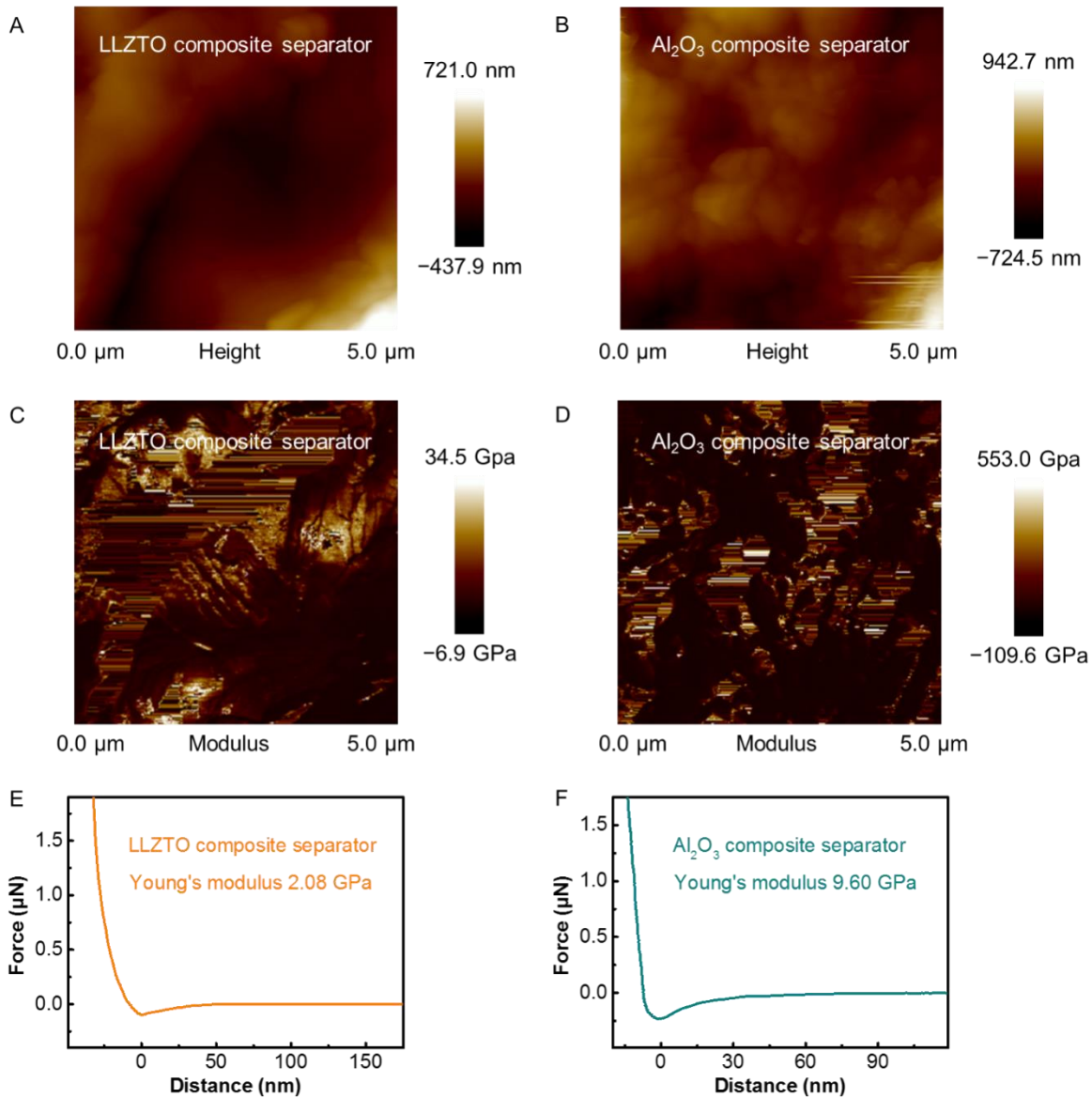red with the LLZTO composite separator of the 5-μm LLZTO film. (**A**) The SEM images of the surface of the separator with thicker LLZTO film. (**B**) A cross-section of the separator exhibiting an overall view consisting of thick LLZTO film and PP matrix. (**C**) Voltage profiles and (**D**) enlarged voltage hysteresis for Li–Li symmetric cells using ether-based DOL/DME electrolytes at a current density of 1.0 mA cm^{-2}.

Fig. S29. Morphology and cycling performances of the separator with isolated LLZTO particles compared with the LLZTO composite separator of the 5-µm LLZTO film. (**A**) The SEM images of the surface of the separator with isolated LLZTO particles, (**B**) A cross-section of the separator exhibiting an overall view consisting of isolated LLZTO particles and PP matrix. (**C**) Voltage profiles and (**D**) enlarged voltage hysteresis for Li–Li symmetric cells using ether-based DOL/DME electrolytes at a current density of 1.0 mA cm^{-2}.
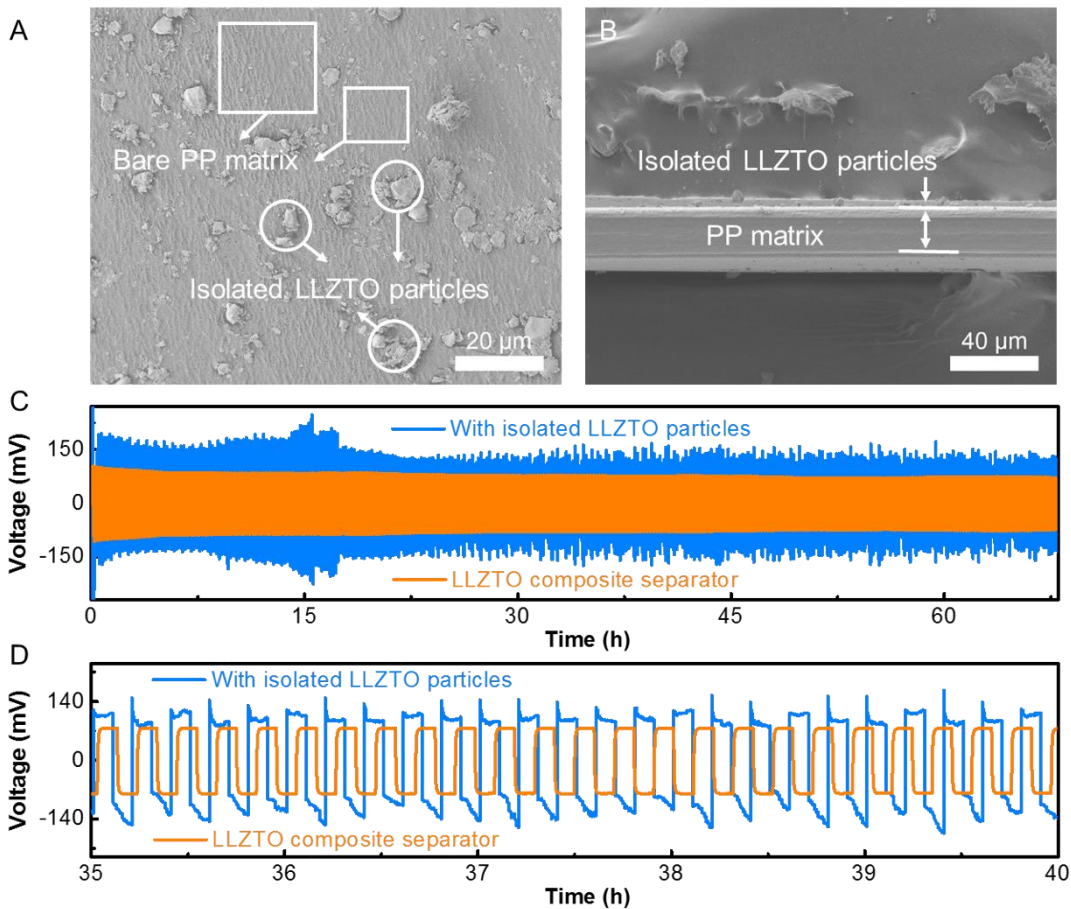
2. Supplementary Tables

Table S1. Statistics of the concentration of Li ions beneath the routine PP separator and the composite separator at $y = 9.0$ μm.

	Concentration of Li ions beneath LLZTO composite separator	Concentration of Li ions beneath routine PP separator
Mean (M)	1.00	1.00
Standard deviation (M)	7.26×10^{-5}	9.76×10^{-4}
Variance (M^2)	5.27×10^{-9}	9.53×10^{-7}
Coefficient of variation	7.26×10^{-5}	9.76×10^{-4}
Range (M)	3.09×10^{-4}	3.37×10^{-3}

Table S2. Element atomic percentage of Li metal anode surface with the LLZTO composite separator and the routine PP separator obtained from XPS spectra.

Element	Atomic %	
	LLZTO composite separator	Routine PP separator
Li	34.2	34.0
C	21.4	20.7
N	0.8	0.3
O	29.7	41.6
F	12.8	3.0
La	0.3	-
Zr	0.07	-